

REPORT DOCUMENTATION PAGE

AFRL-SR-AR-TR-06-0058

Public reporting burden for this collection of information is estimated to average 1 hour per response, including the time for reviewing instructions, data needed, and completing and reviewing this collection of information. Send comments regarding this burden estimate or any other aspect of this burden to Department of Defense, Washington Headquarters Services, Directorate for Information Operations and Reports (0704-0188), 1215 Jefferson Davis Highway, Suite 1204, Arlington, VA 22202-4302. Respondents should be aware that notwithstanding any other provision of law, no person shall be subject to any penalty for failing to comply with a collection of information if it does not display a valid OMB control number. **PLEASE DO NOT RETURN YOUR FORM TO THE ABOVE ADDRESS.**

1. REPORT DATE (DD-MM-YYYY) 20-01-2006		2. REPORT TYPE Final		3. DATES COVERED (From - To) May 1, 2004 - Aug 31, 2005	
4. TITLE AND SUBTITLE Spark Plasma Sintering for Nanostructured smart materials				5a. CONTRACT NUMBER FA 9550-04-1-0343	
				5b. GRANT NUMBER	
				5c. PROGRAM ELEMENT NUMBER	
6. AUTHOR(S) Minoru Taya				5d. PROJECT NUMBER	
				5e. TASK NUMBER	
				5f. WORK UNIT NUMBER	
7. PERFORMING ORGANIZATION NAME(S) AND ADDRESS(ES) Department of Mechanical Engineering, CIMS, University of Washington, Box 352600 Seattle, WA 98195-2600				8. PERFORMING ORGANIZATION REPORT NUMBER CIMS-02-2006	
9. SPONSORING / MONITORING AGENCY NAME(S) AND ADDRESS(ES) Air Force Office of Scientific Research 875 N. Randolph Street, Suite 325 Room Arlington, VA 22203 ATTN: Dr Les Lee, Program Manager				10. SPONSOR/MONITOR'S ACRONYM(S) AFOSR	
				11. SPONSOR/MONITOR'S REPORT NUMBER(S)	
12. DISTRIBUTION / AVAILABILITY STATEMENT unlimited					
DISTRIBUTION STATEMENT A Approved for Public Release Distribution Unlimited					
13. SUPPLEMENTARY NOTES					
14. ABSTRACT This DURIP project is aimed at establishing a new Spark Plasma Sintering (SPS) equipment by which we will be able to process a new set of nano-structured smart materials and composites; shape memory alloy (SMA) composites, ferromagnetic SMA composites, piezo-composites with and without functionally graded microstructure (FGM), a new active materials such as piezo-SMA composites. These composites will be used for higher performance airborne actuators and smart window materials and energy harvesting and cooling materials for airborne antennas.					
15. SUBJECT TERMS					
16. SECURITY CLASSIFICATION OF:			17. LIMITATION OF ABSTRACT	18. NUMBER OF PAGES	19a. NAME OF RESPONSIBLE PERSON
a. REPORT	b. ABSTRACT	c. THIS PAGE			19b. TELEPHONE NUMBER (include area code)

Final Report to AFOSR DURIP (FA9550-04-1-0343)

Spark Plasma Sintering (SPS) for Nanostructured Smart Materials

by

**Minoru Taya, Director
Boeing-Pennell Professor
Center for Intelligent Materials and Systems
Department of Mechanical Engineering
University of Washington, Box 352600
Seattle, WA 98195-2600
Phone: 206-685-2850, Fax: 206-685-8047
Email: tayam@u.washington.edu**

20060309 060



February 5, 2006

DISTRIBUTION STATEMENT A
Approved for Public Release
Distribution Unlimited

Table of Contents.....	Pages
Chapter 1. Abstract.....	1
Chapter 2. Budget	2
2.1. UW budget	2
2.2. Justifications of the budget	2
2.3. Time frame of the installation and multiple user system.....	2
2.4. Technical specifications of the SPS model 1020 S.....	2
Chapter 3. Results of materials processed by SPS	11
3.1. Previous DoD projects	11
3.1.1 Ferromagnetic SMA (Darpa/ONR N00014-00-1-0520, and N00014-02-1-0689).....	11
3.1.2 Hierarchical modeling on Ferromagnetic Shape Memory Alloys (SMA) Composites (AFOSR, F49620-02-1-0028).....	13
3.2. Current DoD projects	17
3.2.1 Design of a porous TiNi with higher energy absorption (Taya, ONR MURI-subcontract).....	17
3.2.2 AFOSR project on Active nano-composites (FA9550-05-1-0196).....	18
(1) New active material of piezo-SMA composites.....	19
(2) Multi-layer functionally graded dielectric materials for microwave applications.....	30
References.....	32

Chapter 1. Abstract

This DURIP project is aimed at establishing a new Spark Plasma Sintering (SPS) equipment by which we will be able to process a new set of nano-structured smart materials and composites; shape memory alloy (SMA) composites, ferromagnetic SMA composites, piezo-composites with and without functionally graded microstructure (FGM), a new active materials such as piezo-SMA composites. These composites will be used for higher performance airborne actuators and smart window materials and energy harvesting and cooling materials for airborne antennas.

The advantage of the SPS system is to lower processing temperature for short processing time, as compared with ordinary sintering furnace, thus, avoiding formation of unwanted intermetallics and larger grain growth achieving higher density materials with sound microstructure, therefore, providing ideal microstructure of nano-structured materials. Due to very short processing time at intermediate to high temperature in inert or vacuum environment, we can expect to process a set of entirely new class of multi-functional composites by using powders of constituent materials without modifying the original properties of the powdered constituents, for example, piezo-SMA composites.

Although a good number of units of SPS have been introduced extensively outside USA; 174 units in Japan, 5 China, 1 Germany, 5 Korea, 1 Singapore, 1 Sweden, there are only two units in North America. Due to this limited access, the University of Washington (UW) team is forced to access to some of the SPS units in Japan, where the UW team is processing ferromagnetic SMA composites and a new class of porous TiNi SMA with high energy absorption. This dependence of outside SPS has slowed down the speed of the UW team research.

The new SPS has already benefited the previous and current DoD projects; (1) previous AFOSR (F4920-2-1-0028) and Darpa/ONR (N00014-00-1-0520) design of ferromagnetic SMA composites for use in higher performance actuators, (2) current AFOSR (FA9550-05-1-0196) design of a new class of active materials such as, piezo-SMA composites which would provide fast responsive and large strain upon applied electric potential, thus harvesting beneficial properties of these constituent active materials, (3) current ONR-MURI subcontract (N00014-02-1-0666) design of a high energy absorbing material based on superelastic property of porous SMA such as TiNi that is processed by SPS. SPS will be used to process a new energy harvesting materials such as thermoelectric materials with higher figure of merit.

There are three faculty at UW who will benefit directly by the SPS, L. Sorensen, Physics who is studying the nanostructure of magnetic materials (including ferromagnetic SMA composites) by XRD, Y. Kuga, EE, who has been characterizing the electric properties of ferroelectric ceramics such as BaTiO₃, and G. Cao, MSE, who has been working on several nanostructured oxide ceramics for use in optoelectrics and actuators.

The SPS system has also been used for training graduate students who are working on AFOSR projects, Mr. O. Namli, Ms. S. Garuraja and Drs. H. Nakayama and Y. Liang. The SPS will be accessed by the engineers at local and regional industries, Boeing (Seattle), and Sienna (Seattle) who are collaborating on several defense related projects. Hourly user fee will be applied to the users within UW and outside users, which is pooled for future maintenance of the SPS.

Chapter 2. Budget

2.1. UW budget

The budget of the proposed SPS is stated below.

- (1) Equipment Purchase
Proposed SPS from Sumitomo Coal Mining Company
which includes 2 day installation & training

The details of the equipment are shown for the next pages.

Total Direct Costs:	33,500,000yen = (\$283,898)
Washington State Sales Tax (8.8%)	\$24,983
<u>1 local shipping cost</u>	<u>\$1,110</u>
Total Cost Requested	\$ 310,000

- (2) UW Matching toward lab renovation \$20,000

2.2. Justifications of the budget

- (1) Purchase of the SPS

The itemized cost of the SPS is listed in the next quotation with total of \$310,000 which includes the cost of initial installation and training of the two senior research associates.

- (2) UW lab renovation cost

The SPS will be installed in MEB G-floor. The SPS requires electric power of 2-15V and 2000A and cooling water line. MEB G-floor will be facilitated with the electric power and cooling water. The total cost estimated for this minor modification is \$20,000.

2.3. Time frame of the installation and multiple user system

The installation of the SPS will start October, 2004 and continues through June 30, 2005. The major calibrations will be done by the end of March 31, 2005, followed by calibrations tailored for several user modes. Two sets of user manual will be made, one is for those students taking lab course (ME/MSE 487) and the other for researchers (graduate students and post docs and faculty). The SPS will be open for outside users, those researchers from collaborating local and regional industries, Boeing, Sienna, and USTLAB.

2.4. Technical specifications of the SPS model 1020 S

The details of the technical specifications and original quotation from the supplier of the SPS system are given on the following pages.

1. System:

Spark Plasma Sintering System
DR. SINTER®
Model SPS-1020

2. Introduction:

DR.SINTER® Model SPS-1020 Spark Plasma Sintering System from Sumitomo Coal Mining Co.,Ltd. is designed for a wide range of experimental research on new materials. The system is based on a new method and a fresh concept: a high performance sintering machine that can still be operated by even personnel without previous experience or training in the field. The DR.SINTER® allows almost anyone to avail themselves of the high levels of powder metallurgy: they can now sinter inorganic materials including ferrous and non-ferrous metals.

SCM's spark plasma sintering process first compresses material the starting powder material, then applies ON/OFF pulse controlled power using the originally developed Sintering DC Pulse Generator to concentrate high density energy positively in the area of neck formation between particles in order to provide compacts with high dimensional accuracy and uniformity.

The SPS system fabricates high-grade sintered compacts at a lower temperature and in a shorter time than conventional sintering methods. Amorphous materials, for example, can be speed-sintered at below the normal temperature of crystallization.

With this process you can control the microstructure of the material and crystal growth, the original properties of the material are maintained. Now with DR.SINTER®, materials previously considered impossible to treat in this way can be sintered.

Sintering can be carried out under atmospheric conditions, with inert gases or even in a vacuum. The system operates over a wide temperature range up to a maximum of 1700°C. DR.SINTER® has optimal functions to aid in development of a broad spectrum of new materials. Sintering and sinter-bonding and joining can be handled for nano phase materials, tungsten carbides, magnetic materials, titanium alloys, amorphous alloys, various electronics materials, functional materials, composites and also fine ceramics. The system can also be used to great advantage with highly porous materials which are normally difficult to sinter.

The DR.SINTER® was designed with special consideration given to the specifications required for ease of use and safety in comprehensive research on new materials.

3. Configuration:

- (1) Sintering Machine Unit
- (2) Sintering DC Pulse Generator and Energizing System
- (3) Vacuum and Hydraulic Unit (Built-in)
- (4) Sintering Operation and Control Unit (Built-in)

4. Main Specification:

4-1 Sintering Machine

- | | |
|------------------------------|--|
| (a) Frame | Tie-bar |
| (b) Sintering Press System | Vertical single axis hydraulic cylinder |
| (c) Maximum Pressure | 100kN {10,200kgf} |
| (d) Sintering Pressure | 5~100kN {510~10,200kgf} |
| (e) Sintering Stroke | 150mm (open height: 250mm) |
| (f) Pressure Control System | Feedback control by proportional solenoid relief valve. Digital readout strain gauge pressure transducer |
| (g) Table size | φ120 mm |
| (h) Sintering Electrode Rods | With special sealed water cooling |
| (i) Z axis position display | Digital readout (min. 0.01mm) |

4-2 Energizing Power Supply and Energizing System

- | | |
|----------------------------------|---|
| (a) Sintering DC Pulse Generator | Peak number control system |
| (b) AC Input | 3 phase, AC200/220V, 50/60Hz
(Matching transformer - not included) |
| (c) DC Output | Pulse output 15V, 2000A |
| (d) Output Range | Voltage 2~15V
Current 0~2000A |
| (e) Control System | Manually operated with volume controlled by digital timer and automatic closed loop program |
| (f) Insulation Conductivity | Over 5MΩ (by DC500V megger) |
| (g) Insulation Limit | AC2000V for 1 minute
(commercial frequency) |
| (h) Energizing System | Connected by special flexible lead wire to internally water-cooled stainless steel rod
(Cable to AC main not included) |
| (i) Sintering Time Setting | 0~99 min. 59 sec. |

4-3 Vacuum and Hydraulic Unit

(a) Vacuum Chamber	Chamber with water cooling jacket with inner double layer stainless steel reflectors
(b) Material	Stainless steel (SUS304)
(c) Dimensions	Inside ϕ 450mm
(d) Vacuum Limit	6Pa (4.5×10^{-2} Torr) (no load)
(e) Exhaust Speed	From air pressure to 6Pa (4.5×10^{-2} Torr) /within 10 minutes
(f) Exhaust System	Rotary pump and Mechanical booster pump
(g) Sintering Ambience	Air, vacuum or inert gas
(h) Viewing Windows	ϕ 50mm & ϕ 80mm quartz glass with individual protecting plates
(i) Vacuum Meters	Combination plus and minus Bourdon pressure gauge and Pirani vacuum gauge
(j) Automatic Temperature Control	PID Digital Programmable Temperature Controller
(k) Temperature Detector	1) Thermocouple (max. temp. 1000°C) detects and digitally display sintering die punch temperature by contact with outside surface. 2) Digital Radiation Thermometer for high temperature range from 600°C to 3000°C. (Option) 1700°C (Option)
(l) Chamber Temperature	Tap water 1.5~3.0 kgf/cm ² , min. 20 lit/min
(m) Cooling Water	

Caution: If the temperature of cooling water should exceed standard value because of operating conditions or frequency of use, promptly correct by force feeding water or installing an exterior heat exchanger.

Note that cooling towers are not provided as standard accessories.

4-4 Sintering Operation & Control Unit

- (a) Power Supply Controller
- (b) Sintering Pressure Controller
- (c) Vacuum System Controller
- (d) Current, Voltage, Oil Pressure and Stroke Indicators
- (e) Temperature Controller

4-5 Standard accessories

- (a) Operation Manuals 2 sets
- (b) Tools 1 set
- (c) SPS Sintering die & punch
 - Graphite (inner dia. ϕ 20mm) 5 sets
 - (" ϕ 30mm) 5 sets
- (d) Graphite spacer 2 sets
- (e) Fuses 1 set
- (f) Lamps 1 set
- (g) Thermocouple (K type) 2 pcs.
- (h) O ring 1 set
- (i) Clamper 1 pc.
- (j) Releasing agent 1 pc.
- (k) Flow indicator 1 pc.

5. Optional Items:

- (1) Digital radiation thermometer
(measuring SPS temperature range 600~3000 $^{\circ}$ C) 1 set
- (2) Analysis Unit 1 set
Consisting of :
 - Specimen displacement ratio measuring equipment
 - SPS Pressure Program Control Unit
 - Gas flow control unit
 - SPS-LCD display system for SPS sintering data analyzing
 - External output terminal
- (3) 1700 $^{\circ}$ C High temperature chamber

6. Utility Requirements:

(1) Electric Power Supply

145A, 50kVA, 3-phase, 200 or 220V(Output guarantee lowest voltage)

(2) Water Supply

Pressure level : 1.5~3 kgf/cm² (0.147~0.294MPa)

Flow rate : more than 20 lit/min.

Water temperature : Under 35°C

7. Standard:

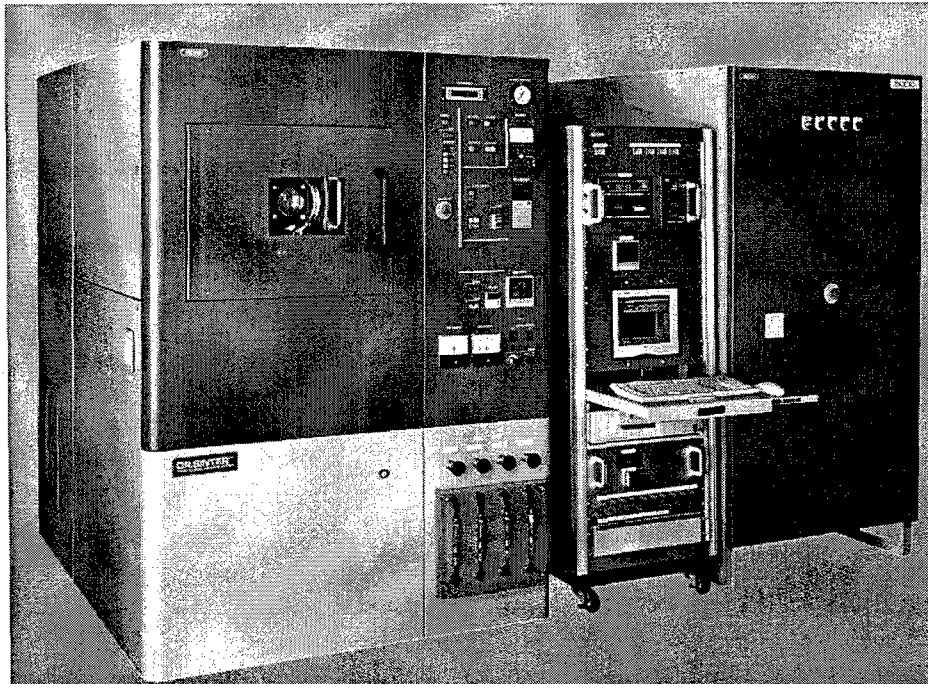
JIS: Japanese Industrial Standard

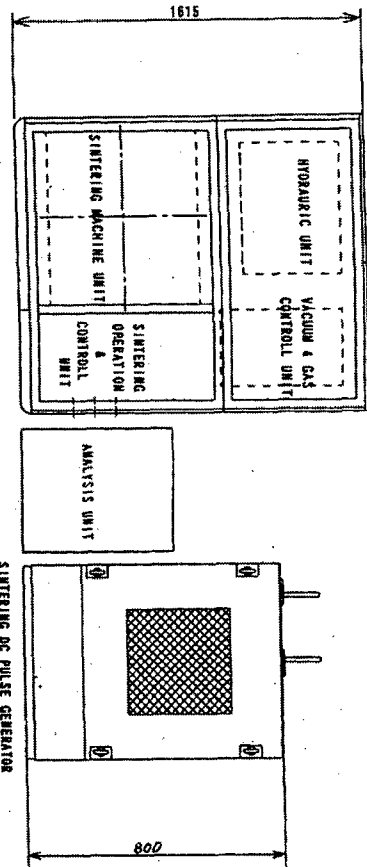
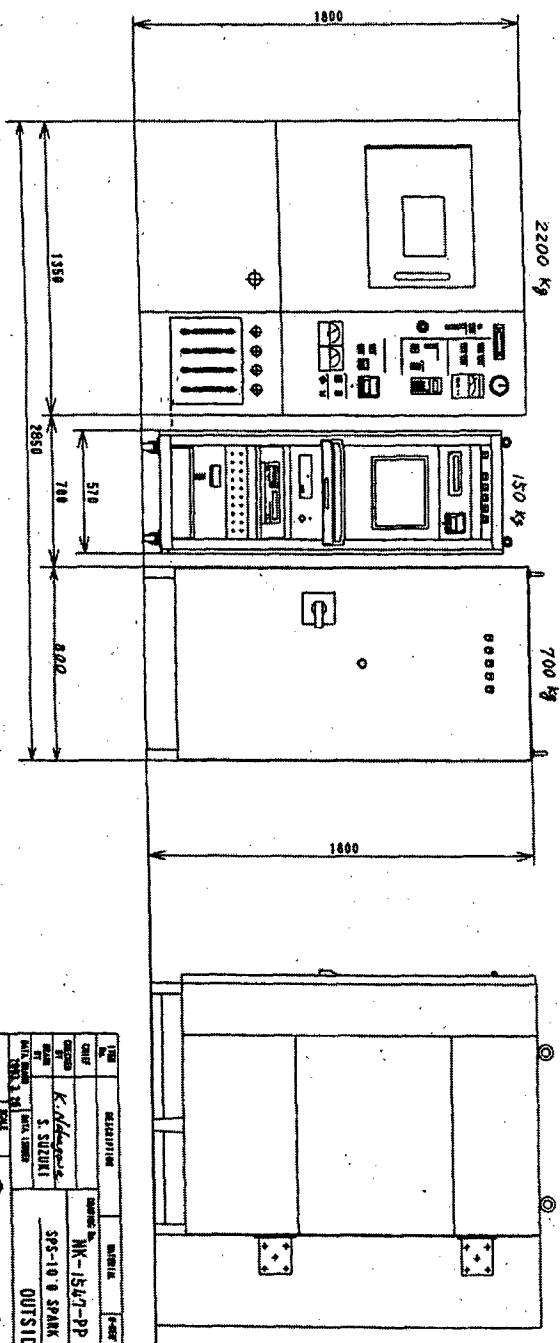
MAS: Standard of Japan Machine Tool Builders' Association

JEC: Standard of The Japanese Electrotechnical Committee

JEM: Standard of The Japan Electrical Manufacturers' Association

OSHA & UL standard compliance is not included





NO	DESCRIPTION	QTY	UNIT	REMARKS
1	SPS-10-8 SPARK PLASMA SINTERING SYSTEM	1	SET	
2	OUTSIDE VIEW	1	VIEW	
<p style="text-align: center;">Sintona Coal Mining Company, Ltd</p>				

Sumitomo Coal Mining Co., Ltd.

29-3, 1-chome, Oji, Kiba-ku, Tokyo 114-8513, Japan
 TEL : (03) 5390-5207, 5208 FAX : (03) 5390-5217

August 8, 2003

Messrs. University of Washington

Offer No. SCM-03-0305

CIF Seattle

A-1. Sumitomo Spark Plasma Sintering System

Dr. Sinter : Model SPS-1020 1 set ¥23,400,000

Consisting of:

- Sintering Machine Unit (Max. Sintering Pressure : 100 kN (10,000 kgf))
- Sintering DC Pulse Generator and Energizing System
(AC Input 3 phases, 200/220V, 50/60Hz, Max. Output: 2000Amps)
- Vacuum & Hydraulic Unit (Built-in)
- Sintering Operation and Control Unit (Built-in)
- Standard Accessories

A-2. Special Specifications and Special Accessories for the Model SPS-1020

1. 1700°C High temperature chamber	1 set	¥2,800,000
2. Digital Radiation Thermometer (Measuring SPS Temperature range 600~3000°C)	1 set	¥1,000,000
2. Analysis Unit	1 set	¥6,300,000

Consisting of:

- Specimen displacement ratio measuring equipment
- SPS pressure program control unit
- Gas flow control unit (mass flow control is available)
- SPS-LCD display system for SPS sintering data analyzing
- External output terminal

Total ¥33,500,000

To be continued

Terms and Conditions

Price : CIF Seattle.
The matching transformer is not included.

Payment : By an irrevocable Letter of Credit at sight in favor of
Sumitomo Coal Mining Co.,Ltd.

Manufacturing Standard : All the SPS systems are designed to comply with Japanese
Industrial Standard(JIS), Standard of Japan Machine Tool
Builders' Association(MAS), Standard of The Japanese Electro
technical Committee(JEC) and Standard of The Japan Electrical
Manufacturers' Association(JEM).
The Systems are also complied with OSHA standard of the USA.
The modification to UL standard compliance is not included .

Warranty : 12 months after installation or 13 months after shipment
whichever comes earlier.

**Installation
& Training** : Installation and tow times trainings by our SPS specialist
at customer's premises are included in the price.

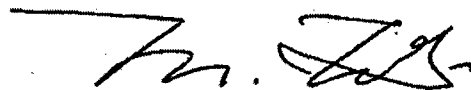
Delivery : Within 5 months after receipt of your firm order.

Packing : Standard export packing

Destination : University of Washington , Seattle, USA

Validity : Till August 31, 2003 inclusive

Remarks : All above terms and conditions are subject to our final confirmation.



M. Tokita
General Manager,
Sintering Systems Department (R & D Center)
New Materials & Processing Division

Chapter 3. Results of materials processed by SPS

3.1. Previous DoD projects

3.1.1 Ferromagnetic SMA (Darpa/ONR N00014-00-1-0520, and N00014-02-1-0689)

The previous DoD project that was helped by this DURIP project on SPS is DARPA/ONR contract "Development of Compact Hybrid Actuators Based on Ferromagnetic Shape Memory Alloys (SMA)" where the program monitors are Dr. R. Barsonum of ONR and Dr. J. Main of DARPA for the period of July 1, 2000 ~ December 31, 2005. The goal of this project is to develop new ferromagnetic shape memory alloys that can be used for robust actuators with large force and displacement capability. Initially we identified a polycrystalline Fe-30.5at%Pd alloy as a key actuator material with its maximum stress of 500MPa and maximum strain of 1%, which can be processed easily into any 3D shapes due to its ductility.

The speed of thermomechanical SMA (such as TiNi) based actuator is limited by the speed of heating and cooling which is of order of 1~10 seconds at best. For most of actuators, faster actuation speed is required as well as higher stress and larger strain capability. In this respect, ferromagnetic SMAs are better actuation materials for fast responsive and robust actuators.

The phase transformation of a ferromagnetic SMA, NiMnGa system, was first reported by Webster et al (1984). Relatively large strain in NiMnGa, induced by applied magnetic field are reported by Ullakko et al (1996) and James and his co-workers (1998, 1999). These large strains induced by the applied magnetic field are the results of rearrangement of martensite variants in the ferromagnetic SMA observed at temperature $T \leq M_f$ (martensite finish). This mechanism is called here "variant rearrangement mechanism". The flow stress level of the ferromagnetic SMA with such large strains induced by the rearrangement of martensite variants is as low as several MPa at operational temperature which is often much lower than room temperature. Also, the level of the applied magnetic field is large (see H_0 in Fig.1(a)) to induced larger strain, requiring large and heavy electromagnets. To design a robust yet compact actuator with large load bearing capacity at room temperature range, one must use a different actuation mechanism associated with phase change of a ferromagnetic SMA

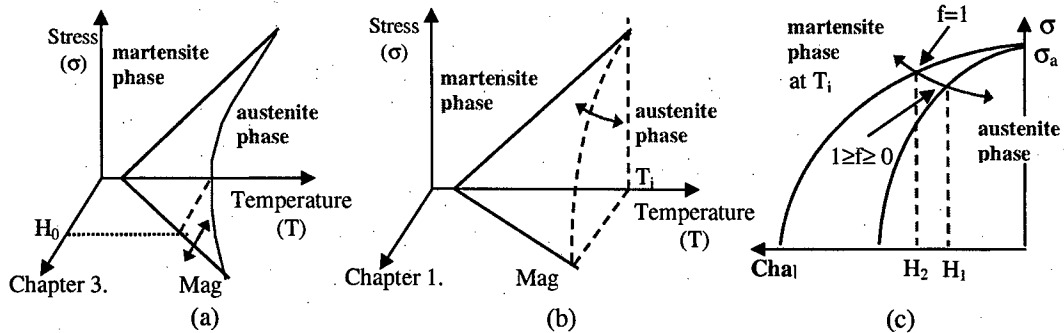


Fig.1 Phase change diagram of a ferromagnetic SMA under stress-temperature-magnetic field loading based on (a) variant rearrangement mechanism and (b), (c) hybrid mechanism, f is martensite volume fraction. (c) is the magnified view of (b) at a constant temperature, T_i .

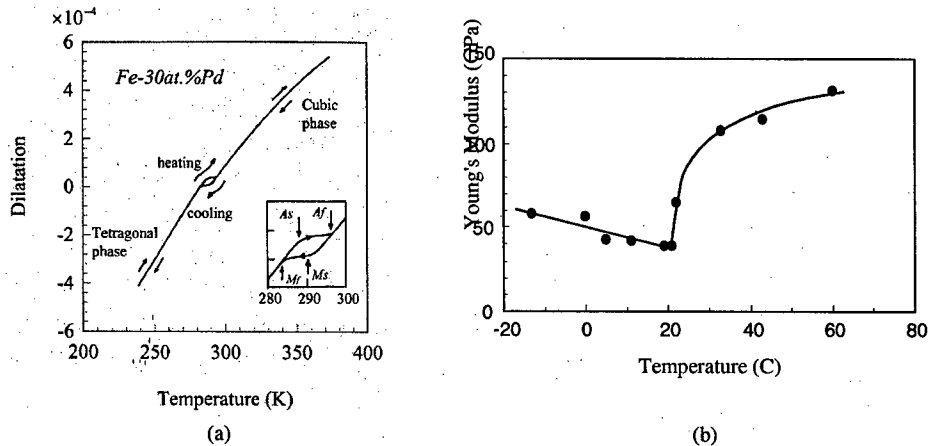


Fig.2 Transformation characteristic of ferromagnetic Fe-Pd system (a) dilatation vs temperature and (b) Young's modulus vs temperature curves

Recently, we (Kato et al, 2002; Kato et al, 2002) proposed a new actuation mechanism for a ferromagnetic SMA, which provides a faster responsive yet powerful actuation, “hybrid mechanism”, which is based on a sequence of chain reactions: first, applied magnetic field H or flux density B with large gradient, inducing large stress field in a ferromagnetic actuator material, prompting stress-induced martensite phase change ($A \rightarrow M$ phase), thus, the elastic properties change from stiff (austenite phase) to softer (martensite phase), as shown in Fig.2(b), resulting in larger displacement. Both the variant rearrangement and hybrid mechanisms are illustrated in a three-dimensional phase change diagram of stress (σ), temperature (T) and magnetic field (H), in Fig.1(a) and (b) respectively, where (c) is the magnified illustration for a constant temperature (T_i), and two solid curves denote the phase boundary of martensite start (inner curve) and finish (outer curve). It is note here that the applied magnetic field based on the hybrid mechanism ($H_2 - H_1$) in Fig.1(c) is normally much less than that based on the variant rearrangement mechanism (H_0 , in Fig.1(a)) and the hybrid mechanism depends on the high gradient of magnetic flux density, enable us to use a compact electromagnet system.

Since ferromagnetic SMA, NiMnGa system, was found to be brittle, and operational under compressive stress field thus not suitable as a robust actuator material, we recently shifted our attention to more ductile ferromagnetic SMAs, Fe-Pd system. To demonstrate a robust actuation of ferromagnetic SMA, Fe-Pd, based on the hybrid mechanism, we performed a bending test of an Fe-Pd specimen and a NiMnGa specimen with a high magnetic field gradient, as shown in Fig.3 where an electromagnet is placed underneath the cantilever beam specimens of Fe-Pd and NiMnGa. Fig.3 clearly demonstrates larger strain induced in the Fe-Pd specimens as compared with the NiMnGa specimen whose bending displacement is nearly zero. The result of Fig.3 implies that Fe-Pd exhibited a large displacement by the hybrid mechanism involving in the stress-induced $A \rightarrow M$ phase change driven by the large magnetic force which is induced by the large magnetic field gradient and also large magnetization of Fe-Pd (1.4T) as compared with smaller magnetization of NiMnGa (0.6T).

Fig.2(a) and (b) show the elongation vs. temperature curve and Young's modulus vs temperature. It is noted in Fig.2(b) that a large change in the Young's modulus of Fe-Pd occurs from austenite to martensite by reducing temperature, or applied stress via stress-induced martensite transformation (the vertical line in Fig.1)

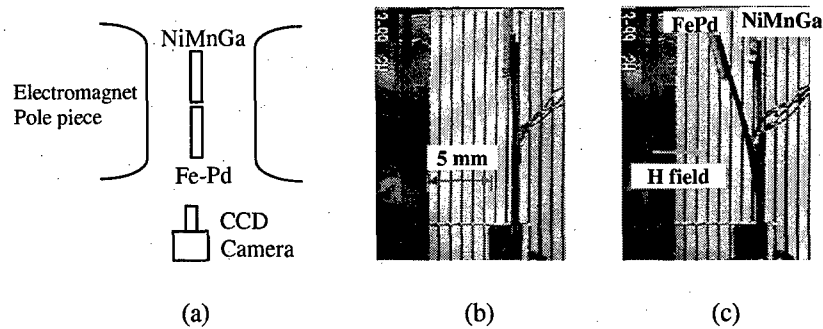


Fig.3 Bending of ferromagnetic cantilever beams, Fe-Pd and NiMnGa, (a) Experimental Setup (b) before applying H-field. Please note that both Fe-Pd and NiMnGa plates are seen as overlapped in this side view (c) bending observed by CCD camera

Despite the successful demonstration of the Hybrid Mechanism applied to ferromagnetic SMA, FePd, the cost of FePd is too high, prompting us to search for a more cost-effective ferromagnetic SMA system. This led us to propose designing of ferromagnetic SMA *composites*, the previous AFOSR project, hierarchical modeling of FSMA composites, the details of which are given in the next section.

3.1.2 Hierarchical modeling on Ferromagnetic Shape Memory Alloys (SMA) Composites (AFOSR, F49620-02-1-0028)

Despite the successful development of high performance ferromagnetic SMA, FePd, the cost of FePd is very high due to the high cost of Pd, preventing us from using FePd to design medium to large sized FePd actuators. To overcome this difficulty, we (Kusaka and Taya, 2003) recently proposed a simple model on ferromagnetic SMA (FSMA) composite which is composed of ferromagnetic material and SMA. The key technology here is to bond these two materials without degradation of both functions, ferromagnetism and SMA behavior (particularly superelastic behavior). The current AFOSR project is aimed at developing several types of high performance FSMA composite for use in designing compact airborne actuators. The basic concept of the FSMA composite is to induce large magnetic force through ferromagnetic materials while utilizing superelastic deformation of a SMA, thus able to carry large force. Examples of FSMA made of ferromagnetic layer and superelastic layer are shown in Figs. 4 (bending plate) and 5 (torsion spring).

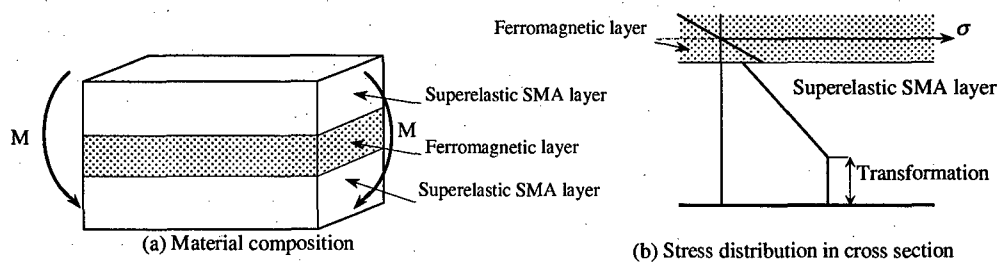


Fig. 4. Composite plate for bending mode actuation.

Fig. 6(a) and (b) show the stress-strain curves of SMA (TiNiCu) and Ferromagnet (FeCoV) plates and the predicted bending moment-curvature relation for several cases of thickness ratio of core ferromagnetic layer to the total composite plate, respectively. The solid line of the bending behavior of FSMA composite plate demonstrates the large superelastic deformation while exhibiting still large bending moment where the outer layers of TiNiCu exhibit superelastic behavior, thus enhancing large bending displacement

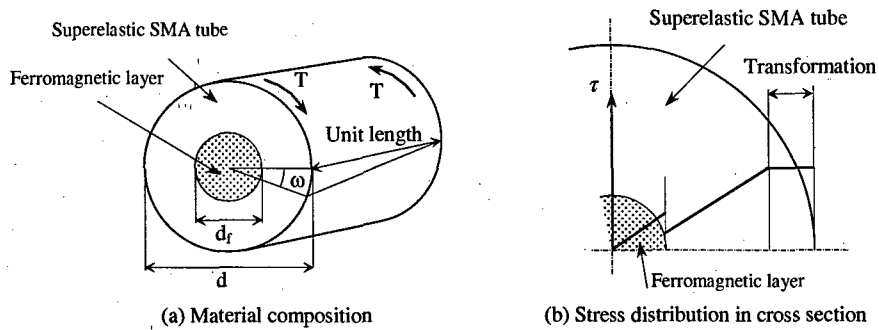


Fig. 5. Composite wire for torsion mode actuation.

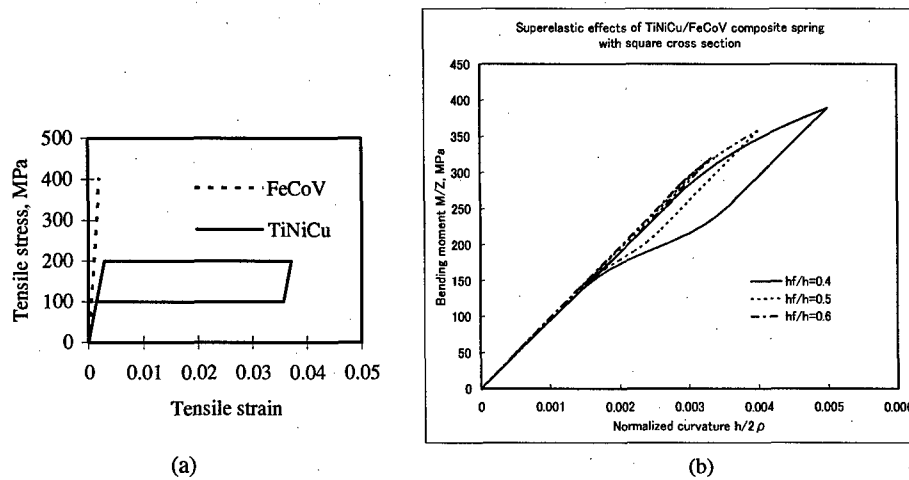


Fig. 6. (a) Stress-strain curves of SMA layer (TiNiCu) and Ferromagnetic layer (FeCoV), (b) the predicted bending movement-curvature relation of TiNiCu/FeCoV/TiNiCu FSMA composite

We attempted to process a FSMA composite laminate by the room temperature vacuum bonding facility at Toyo Kohan Co. Ltd., Japan. Fig.7 shows the cross section of the above composite plate where thin aluminum layer was used as adhesive material. If the surfaces of SMA and ferromagnetic layers are cleaned by plasma-etching in a high vacuum chamber, the bonding of two layers would have been made without Al adhesive layer. Despite limited success of bonding laminated ferromagnetic SMA composite plates, these laminated plates need further heat treatment to convert SMA plate to super elastic grade and ferromagnetic plate to ferromagnetic grade. In the course of such heat-treatment, thin Al bonding layer is softened and

melt, thus destroying the original firm bonding. Thus we are now shifting to use of thin bonding layer metal of higher melting temperature, such as Mo.

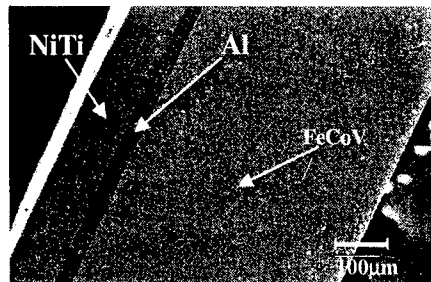


Fig. 7. Cross section of FSMA composite plate (TiNi/FeCoV) where Al thin layer was used as an adhesive.

Alternative design of ferromagnetic SMA composites is use of powder metallurgy processing route. However, ordinary sintering will destroy both properties of ferromagnetic and super elastic behavior of the constituent powdered metals due to longer processing time (several hours) at high temperatures. If ferromagnetic and SMA powders are sintered by the proposed SPS, the microstructure of ferromagnetic SMA is expected to be close to “nanostructured” due to short processing time (typically 2-5 min.) suppressing grain growth. If starting powders are nano-size, the ferromagnetic SMA composite so processed is expected to be higher density (more than 98%). Therefore, the SPS will provide us a great opportunity to design higher performance nanostructured ferromagnetic SMA. The post heat-treatment of the ferromagnetic SMA will be concurrently done as a part of furnace cooling of the SPS.

Several samples of Fe-TiNi composite with varying weight concentrations of constituent powders under various experimental conditions are processed by Spark Plasma Sintering machine newly installed at CIMS, University of Washington, Seattle. (Dr. Sinter SPS-515S, Sumitomo Coal Mining Co., Japan). The SPS machine was installed by DURIP funding under AFOSR Grant The ordinary metallurgical route for processing particulate composites using powder metallurgy i.e., standard sintering produces unwanted reaction products destroying the original properties of SMA and ferromagnet due to elongated processing time at high temperature. In the present work, sintering conducted using the SPS machine consists of applying high temperatures for as short a time as 5 minutes in vacuum accompanied by an applied pressure of around 50 MPa followed by rapid cooling using Argon gas producing remarkably good results. The sintering process is conducted in a vacuum of around 5-6 Pa. These composites after processing are subjected to various characterization tests namely Density Measurement using Archimedes principles, SEM, XRD, DSC, VSM and finally Compression tests. Based on optimizing the SE properties, various SPS temperature conditions, heating rates, volume fractions are tested.

Fig. 8 shows the cross sections of TiNi-Fe composite processed by SPS method where island-shaped phase is TiNi powders of SE grade and continuous phase (matrix) is pure Fe-powders. The magnetization (M) – magnetic field (H) relation of the TiNi-Fe composites with several volume fractions of TiNi are measured and the results are shown in Fig. 9. The magnetization at saturation (M_s) of the composites are measured from Fig. 9 and summarized in Table 1 where the predicted values of M_s by our new analytical model are also shown, resulting in a good agreement. The analytical model for predicting magnetic properties has been already successfully implemented. Fig. 10 shows the compression stress-strain curve of TiNi-Fe composite, showing reasonably good superelastic behavior.

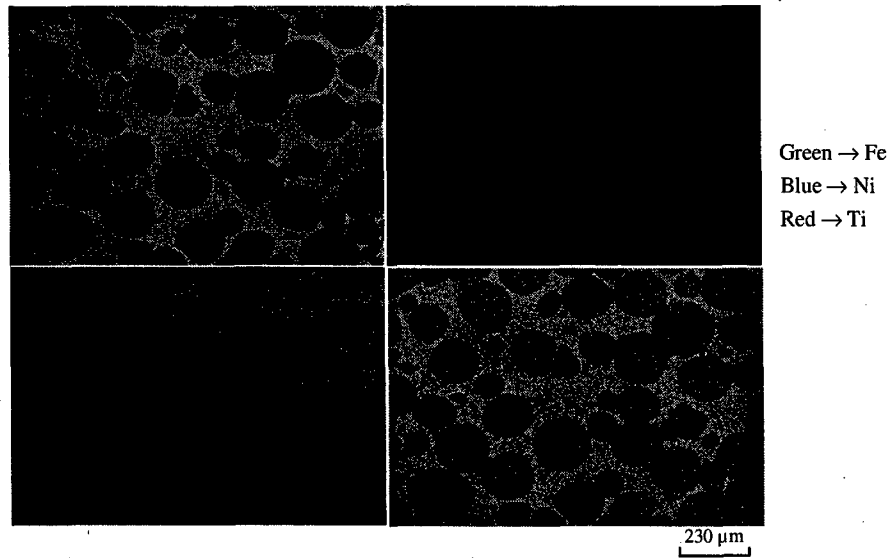


Fig. 8: Composition map of TiNi-Fe composite. Fe is the matrix phase.

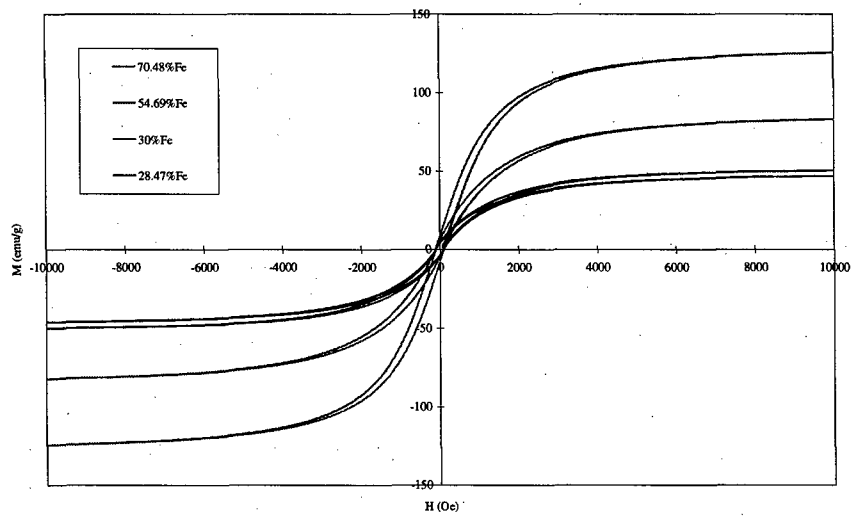
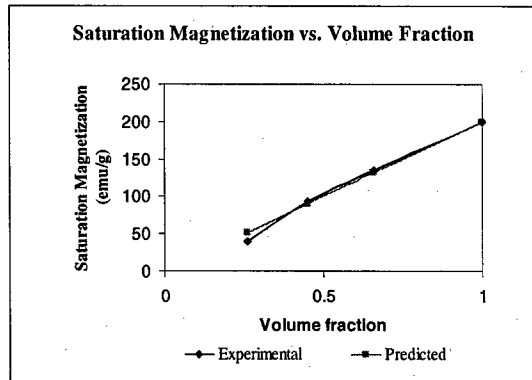


Fig. 9. M-H curve for various TiNi-Fe composites measured using Vibrating Specimen Magnetometer.



Volume fraction (ϕ)	M_s (Experimental)	M_s (Predicted)
0.26133	40	52.266
0.4522	93	90.44
0.6582	135	131.64
1.0	200	200

Table 1. Comparison of Experimental and Predicted Saturation Magnetization values.

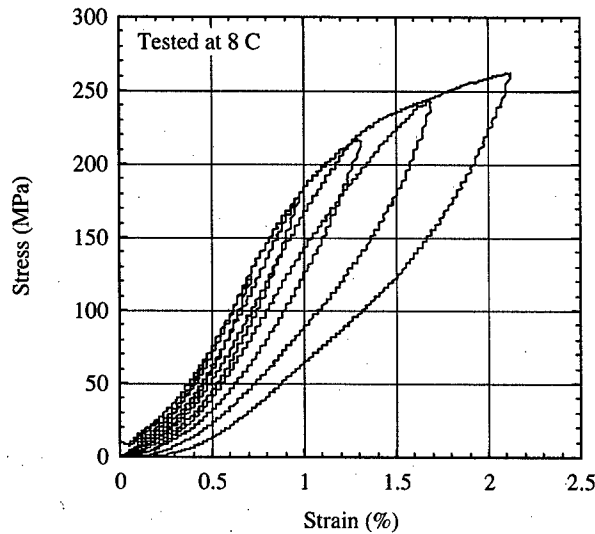


Fig. 10: Compression Stress-Strain curve of TiNi-Fe composite exhibiting SE.

3.2. Current DoD projects

3.2.1 Design of a porous TiNi with higher energy absorption (Taya, ONR MURI-subcontract)

The goal of ONR-MURI project on high energy absorption is to design new materials that exhibit higher energy absorption during compressive impact loading. We proposed to use porous TiNi SMA processed by SPS. TiNi of super elastic grade is known to exhibit large stress-strain curve with higher stress and strain loop, which is an advantage to absorb high impact energy. It is hoped that introduction of porosity in TiNi is to increase the energy absorption capacity/weight and also that the micro-pillar shaped microstructure contributes to the additional energy absorption due to side force effort during micro-buckling of these micro-pillars.

We have processed two different TiNi specimens by spark plasma sintering (SPS) in a collaboration with Tohoku University, Sendai, Japan (Profs. Kang and Kawasaki). The advantage of SPS is to provide strong bonding among TiNi powders of superelastic grades while the powers are subjected to only five minutes, thus avoiding any unwanted reaction products that would be produced by a conventional sintering method. The summary of two TiNi specimens are give in Table 2.

Name	Porosity	Spark Plasma Processing Condition	Transformation Temperature (°C)
Solid TiNi	0	950°C under 50MPa, 5 minutes	$A_s = 18.888$ $A_f = 37.182$
12% porous TiNi	12%	800°C under 25MPa, 5 minutes.	$A_s = 1.288$ $A_f = 24.202$

Table 2. TiNi specimens processed by spark plasma sintering (SPS)

The micro structure of porous TiNi (12% and 25%) are given in Fig.11 (a) and (b)

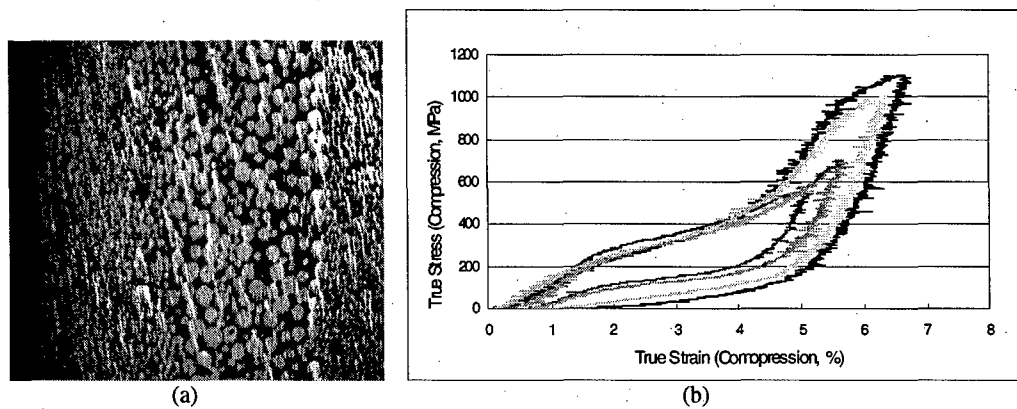


Fig.11. Microstructure of porous TiNi specimens (a) 12% vol. porosity, (b) Superelastic response of porous TiNi under static compression of the specimen with porosity of 12% (Ambient temperature)

Fig. 11(a) shows the cross section of 12% porous TiNi specimen processed by the SPS at Tohoku University, illustrating FGM across the thickness. Fig. 11(b) shows the stress-strain curve of 12% porous TiNi under compression, indicating large super-elastic loop with higher stress and strain level, ideal mechanical behavior for high energy absorption during impact loading.

3.2.2 AFOSR project on Active nano-composites (FA9550-05-1-0196)

This current AFOSR project is aimed at designing a set of new active and sensing materials that are made of nano-structured materials and their composites and it focuses on the following subjects:

- (1) Piezo-SMA composites
- (2) High dielectric materials with functionally graded microstructure
- (3) Thermoelectric materials with higher figure of merit

Applications of (1) are for future airborne actuators, and those of (2) for future microwave antennas and those of (3) for future energy harvesting materials for control of high power of airborne antennas. Preliminary results are obtained only for (1) and (2), thus, their results are given below.

(1) New active material of piezo-SMA composites

Shape memory alloy (SMA) of super elastic grade has a large strain (up to 5% or so) once it is stressed to the stress level of stress-induced martensite transformation, see the plateau stress of Fig. 6(a), while piezoelectrics exhibits small-strain (typically less than 1%) with fast actuation speed under applied electric field. If we combine both SMA powders and piezoelectric powders and process them by the proposed SPS, a new active material of SMA-piezo will be created, which would exhibit larger strain under applied electric field due to the internal stress field by the piezo electric effect. This internal stress field will be transferred to SMA phase, triggering the stress-induced martensite transformation, leading to large super elastic strain, resulting in large actuation strain. In order for this new hybrid mechanism to be valid, the microstructure of the piezo-SMA composite must be such that the piezo-phase forms a percolative network so as to be polarized while SMA phase be isolated, see Fig. 12. The proposed SPS will provide us a capability of processing such a new piezo-SMA composite. Similarly the SPS will be used to process a set of new smart materials that would be possible by the conventional processing method. It is noted here that the SPS can process new target materials such as piezo-SMA which will be sputtered into thin fiber on a given substrate, key MEMS component, as the SPS is ideal to process high density sputtering target materials.

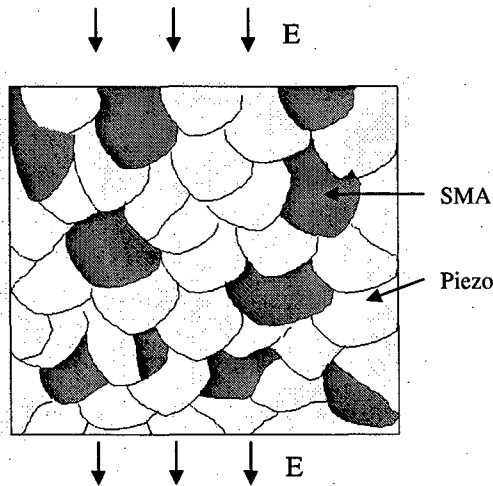


Fig. 12. Microstructure of piezo-SMA composite where the piezo phase (white) forms a percolative network and SMA phase (dark) is isolated island. The piezo-SMA composite is subjected to applied electric field, E.

Piezo-SMA composite is a new concept in taking advantage of both piezoelectric material (fast response under applied E-field) and SMA-SE (large strain under SIM phase transformation i.e., SE deformation). We have made a preliminary design of laminated piezo-SMA composite; Fig. 13 where the top and bottom layers are SMA and middle is piezoelectric material. It is to be noted in Fig.13 that the SMA layers also play the role of electrodes.

To induce larger strain in SMA-SE phase, a constant compressive stress is applied first so as to induce "bias compressive stress" in both piezo and SMA phases in x_1 - direction. Then E-field is applied along the x_3 -direction. We shall explain first the simple 1D model, then 3D model by a new Eshelby's model below.

Case 1 Pre-loading to reach martensite start stress

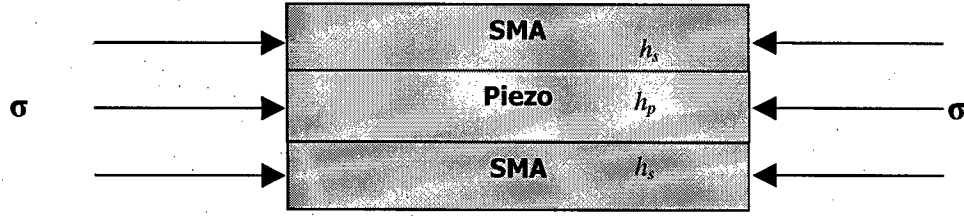


Fig. 13. Composite subjected to applied stress, where h_s : thickness of SMA, h_p : thickness of piezo.

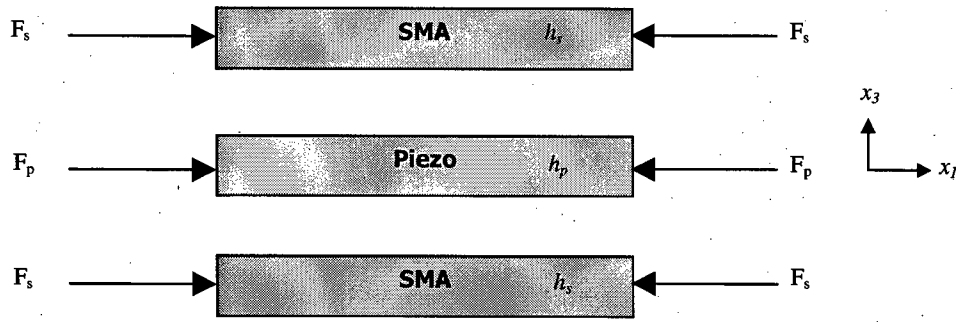


Fig. 14. Free-body diagram for forces acting on each layer.

Force equilibrium:

$$\text{Total force } (F_t): F_t = 2F_s + F_p \quad (1)$$

$$\text{Stress } (\sigma): \sigma = \frac{F_t}{2h_s + h_p} = \frac{2F_s + F_p}{2h_s + h_p} \quad (2)$$

Stress-strain relation:

$$\varepsilon_s = \frac{\sigma_s}{E_s} = \frac{F_s}{E_s h_s} \quad (3)$$

$$\varepsilon_p = \frac{\sigma_p}{E_p} = \frac{F_p}{E_p h_p} \quad (4)$$

Geometric compatibility:

$$\varepsilon_s = \varepsilon_p \quad (5)$$

$$\frac{F_s}{E_s h_s} = \frac{F_p}{E_p h_p} \quad (6)$$

$$\frac{F_p}{h_p} = \sigma_p = \frac{E_p F_s}{E_s h_s} = \frac{E_p}{E_s} \sigma_{ms} \quad (7)$$

σ_{ms} : martensite start stress of SMA

From the above equations, the applied stress to reach stress-induced martensite is computed as

$$\sigma = \frac{2F_s + F_p}{2h_s + h_p} = \frac{F_s}{h_s} \frac{2 + \frac{F_p}{F_s}}{2 + \frac{h_p}{h_s}} = \frac{F_s}{h_s} \frac{2 + \frac{E_p h_p}{E_s h_s}}{2 + \frac{h_p}{h_s}} \quad (8)$$

Since $\sigma_s = \sigma_{ms}$,

$$\sigma_{bias} = \sigma_{ms} \frac{2 + \frac{E_p h_p}{E_s h_s}}{2 + \frac{h_p}{h_s}} \quad (9)$$

$$\epsilon_{bias} = \frac{\sigma_{ms}}{E_s} \quad (10)$$

Case 2 Applied electric field during phase transformation from A to M of SMA

Next, let's consider the constitutive equation of a piezomaterial.

$$\epsilon = S\sigma + dE \quad (11)$$

For one-dimensional case,

$$\epsilon_{11} = S_{1111}\sigma_{11} + d_{31}E_3 \quad (12)$$

where $d_{31} < 0$

With applied stress σ_{bias} , SMA and piezo-material are in equilibrium. With small increase of applied electric field E, stress field in the composite will be changed. The piezo-material tends to be shortened, while the SMA remains unchanged. So, the piezo-material undergoes tension, and the SMA does compression.

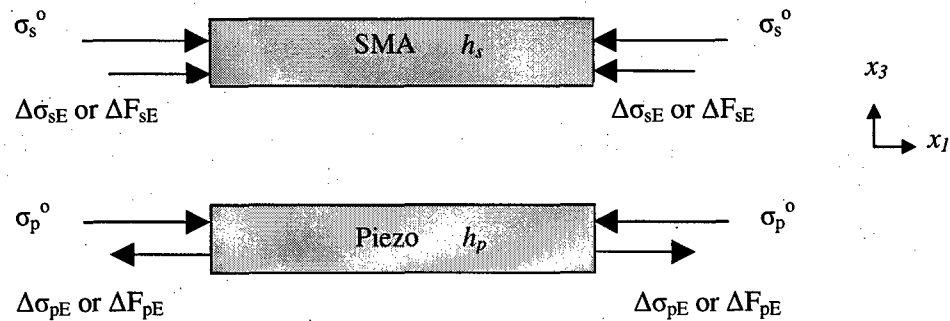


Fig. 15: Free-body diagram with applied stress and applied electric field

Force equilibrium:

$$\Delta F_{pE} = 2\Delta F_{sE} \text{ or } h_p \Delta \sigma_{pE} = 2h_s \Delta \sigma_{sE} \quad (13)$$

Geometric compatibility:

$$\varepsilon_s = \varepsilon_p \quad (14)$$

$$\varepsilon_s^o - \Delta \varepsilon_{sE} = \varepsilon_p^o + \Delta \varepsilon_{pE} \quad (15)$$

Stress-strain relation:

$$\Delta \varepsilon_{sE} = \frac{\Delta \sigma_{sE}}{E_{AM}} \text{ for SMA} \quad (16)$$

$$\varepsilon_{pE} = S_{1111}(\sigma_p^o + \Delta \sigma_{pE}) + d_{31} \Delta E_3 \text{ for piezomaterial} \quad (17)$$

$$\varepsilon_p^o + \Delta \varepsilon_{pE} = \frac{1}{E_p}(\sigma_p^o + \Delta \sigma_{pE}) + d_{31} \Delta E_3 \quad (18)$$

Introducing Eqs. (10) and (12) into (9),

$$-\frac{\Delta \sigma_{sE}}{E_{AM}} = \frac{\Delta \sigma_{pE}}{E_p} + d_{31} \Delta E_3 \quad (19)$$

Eq. (7) is reduced to

$$\Delta \sigma_{sE} = \frac{h_p}{2h_s} \Delta \sigma_{pE} \quad (20)$$

By inserting Eq. (14) into (13),

$$-\frac{1}{E_{AM}} \frac{h_p}{2h_s} \Delta \sigma_{pE} = \frac{\Delta \sigma_{pE}}{E_p} + d_{31} \Delta E_3 \quad (21)$$

Rewriting Eq. (21),

$$\left(-\frac{1}{E_p} - \frac{1}{E_{AM}} \frac{h_p}{2h_s} \right) \Delta \sigma_{pE} = d_{31} \Delta E_3 \quad (22)$$

Thus, the incremental stress induced by the applied electric field is given by

$$\Delta \sigma_{pE} = \frac{d_{31} \Delta E_3}{-\frac{1}{E_p} - \frac{1}{E_{AM}} \frac{h_p}{2h_s}} \quad (23)$$

The strain induced by the applied electric field is obtained as

$$\varepsilon_p = \varepsilon_p^o + \Delta \varepsilon_{pE} = \varepsilon_{bias} + \frac{\Delta \sigma_{pE}}{E_p} + d_{31} \Delta E_3 \quad (24)$$

We propose an Eshelby type model to analyze the newly designed Piezo-SMA composite, Fig.16.

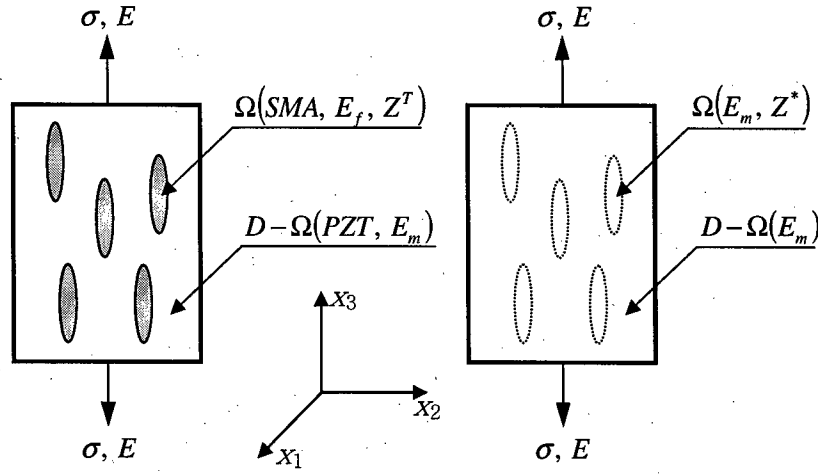


Fig.16. Piezo-SMA composite

Eshelby's Model for Piezo-SMA Composites

i. Formulation

The composite is piezoelectric matrix, reinforced with discontinuous shape memory alloy fibers, as shown in Fig. 16.

The constitutive equations for piezoelectric materials are written as

$$\Sigma = EZ \quad (25)$$

where $\Sigma = \begin{bmatrix} \sigma \\ D \end{bmatrix}$, $E = \begin{bmatrix} C & e \\ e & -k \end{bmatrix}$, $Z = \begin{bmatrix} \varepsilon \\ -E \end{bmatrix}$, and σ , D , C , e , κ , ε , and E denote stress, electric displacement, stiffness, piezoelectric constant, dielectric constant, strain, and electric field, respectively.

Initially applied stress of σ^o and electric field of $E = 0$ (Case I)

The composite is subjected to the applied stress only, $V_{appst} \sigma^o$, with zero electric field. The magnitude of the initially applied stress to the composite is just to initiate stress-induced martensite transformation of SMA fiber. Mixed boundary conditions of stress and electric field imposed on the composite are converted into non-mixed boundary conditions of stress and electric displacement by using the composite properties derived by Dunn et al. Its electroelastic moduli E_c are expressed as

$$E_c = E_m \{I + fD(E_f - E_m)\} \quad (26)$$

where $D = \{(1-f)(E_f - E_m)S + E_m\}^{-1}$, I , E_m , E_f , S and f denote identity matrix, electroelastic moduli of matrix and fiber, piezoelectric Eshelby tensor, and volume fraction of fiber, respectively.

By using the boundary conditions, the strain of the composite, \mathcal{E} , can be computed as:

$$\mathcal{E} = C^{-1}\sigma = C^{-1}V_{appst}\sigma^o \quad (27)$$

The electric field of the composite, D , can be derived as:

$$D = e\mathcal{E} = eC^{-1}V_{appst}\sigma^o \quad (28)$$

Non-mixed boundary condition of stress and electric displacement imposed on the composite is expressed as

$$\Sigma^o = \begin{bmatrix} \sigma \\ D \end{bmatrix} = \begin{bmatrix} V_{appst} \\ eC^{-1}V_{appst} \end{bmatrix} \sigma^o = V_{\Sigma^o} \sigma^o \quad (29)$$

When subjected to a far-field uniform load Σ^o , the stress and electric displacement in the inhomogeneity, Σ_f , can be written as:

$$\Sigma_f = E_f(Z^o + \bar{Z} + Z - Z^*) = E_m(Z^o + \bar{Z} + Z - Z^*) \quad (30)$$

Under the same condition, the stress and electric displacement in the matrix, Σ_m , can be written as:

$$\Sigma_m = E_m(Z^o + \bar{Z}) \quad (31)$$

The disturbed strain and electric field in the inclusion, Z , are related with fictitious eigenfields Z^* through piezoelectric Eshelby tensor S as:

$$Z = SZ^* \quad (32)$$

Since the non-mixed boundary condition is Σ^o , the average strain and electric field are expressed as:

$$\bar{Z} + f(Z - Z^*) = 0 \quad (33)$$

Z^* is computed as

$$Z^* = -B(E_f - E_m)Z^o \quad (34)$$

where $B = \{(E_f - E_m)[(1-f)S + fI] + E_m\}^{-1}$.

The total strain and electric field in the composite are computed by taking volume integral as:

$$Z_c = (1-f)Z_m + fZ_f = Z^o + fZ^* \quad (35)$$

The stress and electric displacement in the fiber domain are expressed as

$$\Sigma_f = V_{\Sigma_f} \sigma^o \quad (36)$$

where $V_{\Sigma_f} = [E_m - (1-f)E_m(S-I)B(E_f - E_m)]E_m^{-1}V_{\Sigma^o}$.

The magnitude of initially applied stress to initiate austenite to martensite transformation of the fibers, σ_{ms}^o , can be determined as

$$\sigma_{ms}^o = \frac{\sigma_{ms}}{V_{\Sigma_f,3} - V_{\Sigma_f,1}} \quad (37)$$

where σ_{ms} represents martensite start stress of the fiber.

Initially applied stress of σ^o and electric field of E (Case II)

During transformation stage of austenite to martensite, the relation between stress and strain of the SMA fiber is assumed to be linear. The applied stress is kept to be constant and electric field, E , are varied. The magnitude of applied stress is computed from Eq. (37). The electric field is increased to fully transform SMA fibers from austenite to martensite. Case II is the superposition of the electric field E on Case I, so the composite under E is analyzed. Its results are superposed on the results obtained in Case I.

At an arbitrary electric field, E , the mixed boundary condition is converted into non-mixed boundary condition with the same procedure mentioned in Case I. The electric field of the composite, D , can be derived as:

$$D = eC^{-1}eE + \kappa E \quad (38)$$

Non-mixed boundary condition of stress and electric displacement is expressed as

$$\Sigma^o = \begin{bmatrix} \sigma \\ D \end{bmatrix} = \begin{bmatrix} 0 \\ eC^{-1}eV_{ef} + \kappa V_{ef} \end{bmatrix} E^o = V_{E^o} E^o \quad (39)$$

The stress and electric displacement in the fiber domain are expressed as

$$\Sigma_f = V_{\Sigma_f, E^o} E^o \quad (40)$$

where

$$V_{\Sigma_f, E^o} = E_f \{ I + [(1-f)S + fI](-B)(E_f - E_m) \} E_m^{-1} V_{E^o},$$

and

$$B = \{ (E_f - E_m)[(1-f)S + fI] + E_m \}^{-1}.$$

The magnitude of applied electric field for the fibers to reach the martensite finish, E_{mf}^o , is determined as:

$$E_{mf}^o = \frac{\sigma_{mf}}{V_{\Sigma_f, E^o, 33} - V_{\Sigma_f, E^o, 11}} \quad (41)$$

With computed E_{mf}^o and Eqs. (35), the total strain of the composite is computed under E only. Finally, the total strain of the composite is sum of the strains induced by both Cases I and II.

Piezoelectric material only (Case III)

The relation between strain and electric field of the piezoelectric material under the same condition of Case I and II is computed by Eq. (26).

ii. Sample calculations

In this study, the composite is short CuMnAl fiber reinforced PZT matrix composite, whose properties are as follows. The magnitude of applied stress to initiate martensite start of the fiber is calculated to be 154 Mpa, and the relations between the strain and electric field of the composite and PZT only are predicted and are shown in Fig. 17.

Fiber: CuMnAl

Aspect ratio=10, Volume fraction=0.1, Austenite Young's modulus=29.5Gpa, Martensite Young's modulus=5.75Gpa, A to M Young's modulus=1.78Gpa, Poisson's ratio=0.3, Dielectric constant $\kappa=1$, Martensite start stress=117Mpa, Martensite finish stress=217Mpa, Transformation strain=0.056226

Matrix: PZT

$C_{11} = 146GPa$, $C_{12} = 95.4GPa$, $C_{13} = 94.3GPa$, $C_{33} = 128GPa$, $C_{44} = 25.3GPa$
 $e_{31} = -3.94$, $e_{33} = 17.5$, $e_{15} = 12.3$, $d_{31} = -164.29 \times 10^{-12}$, $d_{33} = 378.79 \times 10^{-12}$,
 $d_{15} = 486.17 \times 10^{-12}$, $\kappa_{11} = 916$, $\kappa_{33} = 1654$

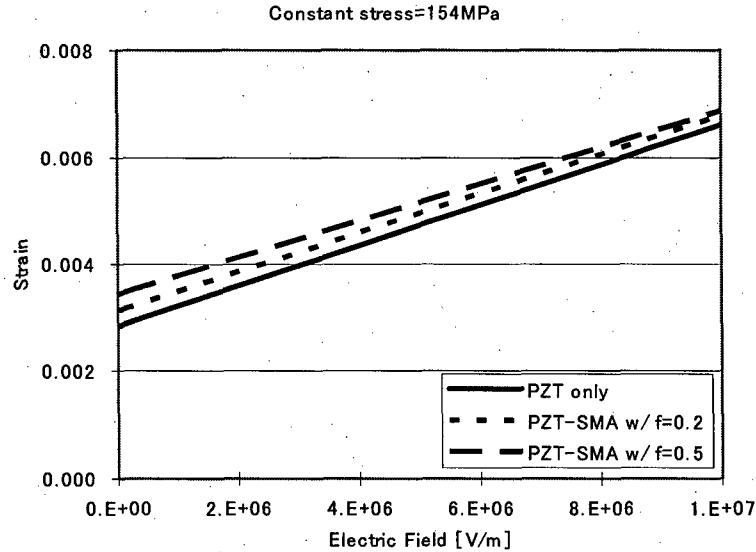


Fig.17. Strains of the PZT-SMA composite and PZT only as a function for electric filed

We attempted to process piezo-SMA laminated composites first using powders of piezo and SMA (TiNi), Fig.18(a). However, piezo powders (PMN) were oxidized during high temperature SPS process, and became darkened, thus losing piezo properties. In order to recover the piezo properties, we had to apply reduction process, i.e. heat treatment in a reducing environment. This post heat treatment in reducing environment resulted in the composite with poor piezo properties. Therefore we tried next by using piezo-plate and TiNi plates stacked together, then subjecting the laminate to SPS process, Fig.18(b). The advantage of this method is to keep the original properties of both piezo (PZT) and TiNi plates, while the disadvantage is difficulty of making a stronger bonding between piezo plate and TiNi plate. This method resulted in often in cracking of PZT plate that presumably was caused during pressurizing of SPS process, and brittle nature of PZT plate. Therefore, we switched to third method, Fig.18(c) where two SMA rings are introduced in the middle layer that constraint PZT piezo disc. In addition, we inserted TiNi powders at the interface between TiNi plates and Piezo disc. Upon SPS process, the piezo-SMA laminate composite, Fig.18(c) appears to be good in shape, no blackening, and no cracking.

All cases of methods, (a), (b) and (c) in processing of piezo-SMA laminates, are summarized in Table.3, where the best piezo-SMA composite is named as case 8. The cross section of case 8 is shown in Fig.19.

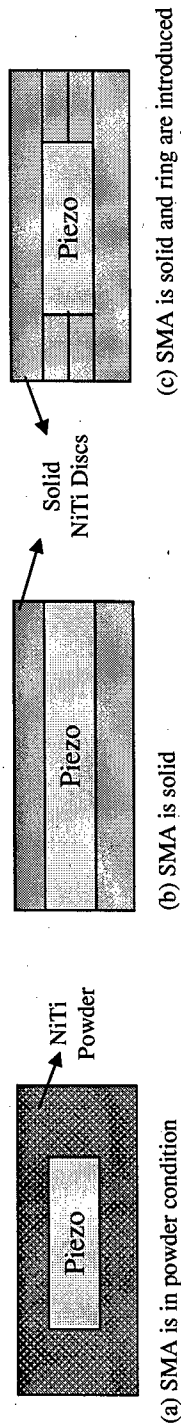


Fig. 18. Schematic view for preparing the specimen for SPS process

Case	Pressure (MPa)	Heating rate (°C/min), Peak Temp (°C)	Time (min)	Piezo (dia, thickness) mm	TiNi disc, (dia, thickness) mm	TiNi ring, thickness mm	Setup (Fig. 18)	Results
1	1.60	100, 800	5	PMN (20, 1.05)	Powder (fine)	N/A	a	PMN color is OK. Several axial cracks. Low porosity, due to fine powder.
2	12	100, 800	5	PZT (10, 2.05)	(10, 1)	N/A	b	PZT is broken. Pressure is high.
3	3.6	100, 800	5	PMN (20, 1.05)	(20, 1)	N/A	b	PMN is broken; one surface is bounded well, while the other is not. PMN get black in color.
4	7.96	100, 800	5	PZT (10, 2.05)	(30, 1)	2x1	c	PZT is broken. Rings are not bounded; also PZT is not bounded to TiNi. Surface polishing should be better.
5	4.6	100, 800	5	PZT (10, 2.05)	(30, 1)	2x1	c	Total thickness of the rings is equal to the PZT thickness. PZT is broken. Bounding is OK, between PZT and TiNi.
6	0.80	100, 800	5	PMN (20, 1.05)	Powder, fine around the PMN and SMA contact surfaces; 300µm in the top and bottom of the die.	N/A	a	Low range pressure is used for the first time. Only one crack observed in the axial direction. High porosity due to thick powder.

Case	Pressure (MPa)	Heating rate (°C/min), Peak Temp (°C)	Time (min)	Piezo (dia, thickness) mm	TiNi disc, (dia, thickness) mm	TiNi ring, thickness mm	Setup (Fig. 18)	Results
7	1.11	100	5	PMN (20, 1.05)	(20, 1)	N/A	b	PMN is broken on purpose before SPS in order to figure out difference in color through the cracks. After the experiment, it is observed that some axial and radial cracks; color is black so the difference can not be observed. One side is bounded well while the other is not.
8	1.11	100	5	PZT (10, 2.05)	(30, 1)	2x1	c	Low range loading, PZT with 2.05 mm thickness is used. Fine powder is applied in the gaps between the PZT and Discs due to the thickness difference in PZT and Rings. Also fine powder is applied between TiNi contact layers. Color is OK. No cracks. Bounding seems OK, but should be examined by removing the solid TiNi parts.

Table 3. Summary of SPS processing on piezo-SMA laminates.

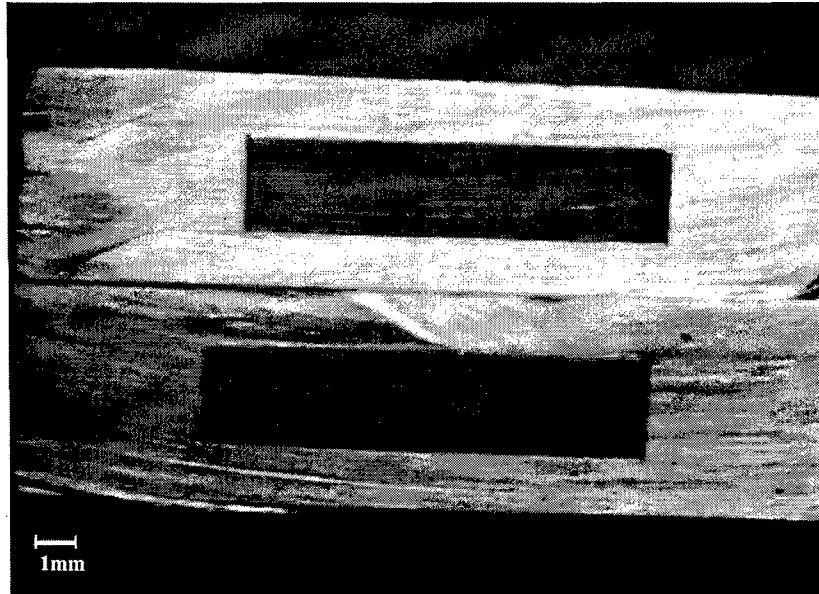


Fig. 19. Cross section of PZT-TiNi laminated composite processed in case 8 of Table 3.

(2) Multi-layer functionally graded dielectric materials for microwave applications

There has been an increasing interest in controlling microwave/millimeter-wave dielectric properties of materials by introducing micro- and macro- structures into a host material. One example is photon-gap materials which use the man-made 2-D and 3-D crystal structures to control the wave propagation characteristics. A patch antenna with the photon-gap structure to control the surface wave has been successfully demonstrated.

Another example is non-uniform very high- ϵ_r dielectric materials. High- ϵ_r materials such as barium-titanate BaTiO_3 ($\epsilon_r = 37$ at 6 GHz) are widely used for wireless devices as a substrate of miniature-sized antennas and dielectric resonators. The typical antenna has a dimension such as patch length and line length of approximately $\lambda/2$ to $\lambda/4$ where λ is the wavelength inside the substrate. Because most wireless systems operate at a lower microwave region with a fairly long wavelength, it is important to fabricate antennas on a non-uniform high- ϵ_r substrate to reduce the physical dimension. The antenna size can be reduced by optimizing (or functionally grading) the material properties around the radiating elements. There have been significant DoD and industry efforts to reduce the size of microwave antennas in recent years. Small, rugged, low-profile antennas can be mounted on military uniforms, helmets, and vehicle surfaces.

It has been suggested that the conductor loading method can also be used for creating high dielectric constant materials. The main problem, however, is when the low-loss host material is loaded with conducting particles; both real and imaginary parts of complex dielectric constant tend to increase. The resulting complex dielectric constant depends on the fractional volume, size and shape, and conductivity of inclusions. Recently, we have demonstrated that the dielectric constant can be increased up to 30% by loading titania ($\epsilon_r = 96$ at 6 GHz) with platinum particles as shown in Fig. 20. (Kuga et al, 2002; 2005). Unfortunately, the test samples were processed with the hot-pressing technique which limited the choice of conducting particles. In addition the traditional ceramic processing method such as ordinary sintering does not allow the fabrication of

predetermined geometric structures. Based on our numerical studies, we have found that the dielectric constant can be increased by properly orienting particles of identical shape and size. The proposed SPS will allow us to fabricate materials with different compositions. By using masks we will be able to embed desired particle shapes and sizes into a host material.

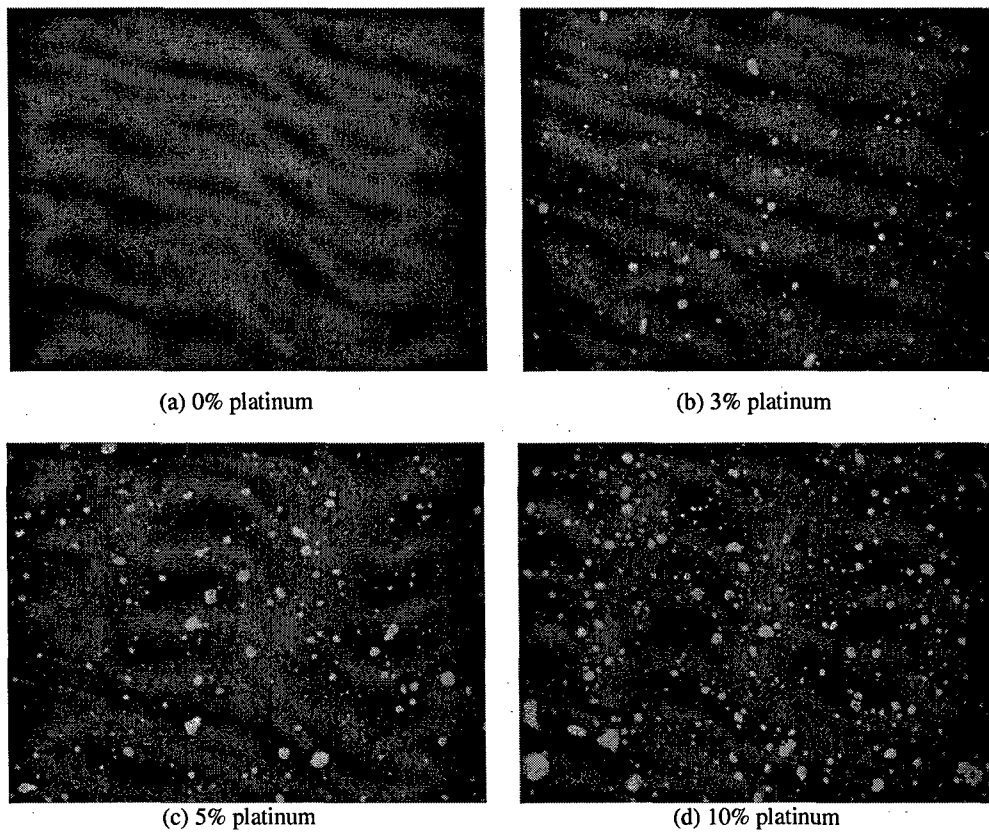


Fig. 20. Micro-structural view of BaTiO_3 platinum composites.

References

- Fenter, P., Geissbuhler, P., DiMasi, E., Srajer, G., Sorensen, L.B., and Sturchio, N.C., 2000, *Geochimica et Cosmochimica Acta* 64, pp.1221.
- Hu, B., Geissbuhler, P., Sorensen, L.B., Kevan, S.D., Kortright, J.B., and Fullerton, E.E., 2001, *Synchrotron Radiation News*, 4:2, pp.11.
- IEEE Spectrum, Technology 2001 Analysis and Forecast, Jan. 2001.
- James, R.D. and Wutting, M., 1998, *Phil. Mag.* A77, 1273-1299.
- Kato, H., Liang, Y., and Taya, M., 2002, *Scripta Materialia*, 2002, 46, pp471-475.
- Kato, H., Wada, T., Liang, Y., Tagawa, T., Taya, M., and Mori, T., 2002, *Mater Sci Eng-A*, A332, pp134-139.
- Kinomura, T., Nasu, S., Kanekiyo, H., and Hirosawa, S., 1997, *J. Japanese Inst. Metals*, vol. 61(2), p184
- Kneller, E.F., and Hawig, R., 1991, *IEEE Trans. Magn.*, vol. 27, p2588
- Kuga, Y., Lee, S.W., Almajid, A., Taya, M., Li, J.F., and Watanabe, R., 2002, "Experimental and Numerical Studies of Microwave Properties of BaTiO₃-Pt Composites", SPIE Meeting, Seattle, Washington, July 7-11.
- Kuga, Y., Lee, S.W., Taya, M., Almajid, A., Lee, S., Li, J.F., and Watanabe, R., 2005, *IEEE Trans on Dielectrics and Electrical Insulation*, vol 12 (no.4), pp827-834.
- Kusaka, M., and Taya, M., 2003, submitted to *J. Composite Materials*, Design of Ferromagnetic Shape Memory Alloy Composites
- Kusaka, M., and Taya, M., *J Composite Materials*, vol 38, no. 12: 1011-1035 (2004)
- Matsui, M., Shimizu, T., Yamada, H., and Adachi, K., 1980, *J.Mag.Mag.Mater.*, 15-18, 1201-1202.
- Sohmura, T., Oshima, R. and Fujita, F.E., 1980, *Scripta Met.* 14, 855-856.
- Sturchio, N.C., Chiarello, R.P., Cheng, L.W., Lyman, P.F., Bedzyk, M.J., Qian, Y.L., You, H.D., Yee, D., Geissbuhler, P., Sorensen, L.B., Liang, Y., and Baer, D.R., 1997, *Geochimica et Cosmochimica Acta* 61, pp.251.
- Tickle, R. and James, R.D., 1999, *J. Magnetism, Mag. Mater*, 195, 627-638.
- Ullako, K., Huang, J.K., Kantner, C., O'Handley, R.C., and Koin, V.V., 1996, *Appl. Phy. Letts.*, 69, 1966-1968.
- Webster, P.J., Ziebeck, K.R.A., Town, S.L. and Peak, M.S., 1984, *Phil. Mag.*, B49, 295-310
- Y.Mikata. *International Journal of Solids and Structures*. 38 (2000) 7045-7063.
- J.D.Eshelby. *Proceedings of the Royal Society of London. Series A, Mathematical and Physical Sciences.* (1957) 241, 376-396.
- J.D.Eshelby. *Proceedings of the Royal Society of London. Series A, Mathematical and Physical Sciences.* (1959) Vol. 252, 561-569.
- T.Mori and K.Tanaka. *Acta Metallurgica.* (1973) Vol. 21:571-574.